Design of Saliency-Based Sensorless-Controlled IPMSM With Concentrated Winding for EV Traction

Myung-Seop Lim, Seung-Hee Chai, and Jung-Pyo Hong

Department of Automotive Engineering, Hanyang University, Seoul 133-791, Korea

This paper investigates the influence of the geometry design parameters of an interior permanent magnet synchronous motor with concentrated winding on the saliency-based sensorless drive feasibility. To evaluate the sensorless controllability of the motors, two different methods to estimate the rotor position error are proposed. By using the methods, the geometry design parameters in the stator are analyzed to figure out which ones have a positive effect on the sensorless drive. The analysis results show that the configuration of the tooth tip is one of the major factors in reducing the estimation error. Based on the results, an optimum design parameter is selected considering both the drive feasibility and the back electromotive force. Last, a final model is proposed and manufactured for electric vehicle traction. The validity of the proposed estimation methods and the design result are verified by the experiments.

Index Terms— **Inductance, permanent magnet (PM) motors, sensorless control, total harmonic distortion (THD), traction motor.**

I. Introduction

TODAY, an interior permanent magnet synchronous motor (IPMSM) is usually employed as electric vehicle (EV) traction because of its high torque density [1]. To achieve the best performance of the machine, a position sensor is essential. However, this increases system cost, volume, and complexity, and decreases the reliability of the machine. In addition, the sensors are not durable enough to operate normally under severe environment conditions in vehicles. This concern is coming to the fore, because if the sensors are faulty, the driver cannot control the vehicle. For these reasons, the design method of a sensorless-controlled motor is a critical goal not only for system cost and volume reduction but also for fault-tolerant control feasibility.

Speed-dependent back electromotive force (BEMF)-based sensorless control cannot be used in the zero- and low-speed ranges, because the magnitude of BEMF is extremely small. Therefore, based on saliency, the rotor position can be estimated by measuring the current response or variation of the inductance with high-frequency voltage injection [2]. It is hard to estimate the rotor position under heavy load conditions, however, because the responses are distorted by the saturation effect and harmonics [3]–[6]. This problem becomes more apparent when the concentrated winding is applied to a motor, but there are only a few papers focusing on the path optimization of q-axis of the rotor [3], [7]. If the shape of the stator is only changed, there is no need to repeatedly conduct rotor stress analysis. In addition, the cost and the time needed to obtain and fabricate the PMs can be reduced when there is a manufactured reference machine, because the rotor of the reference machine can be used as it is in [8]. However, it is hard to find suitable prior research on design methods using the design parameters in the stator.

Manuscript received June 27, 2015; revised August 6, 2015; accepted August 25, 2015. Date of publication August 27, 2015; date of current version February 17, 2016. Corresponding author: J.-P. Hong (e-mail: hongjp@hanyang.ac.kr).

Color versions of one or more of the figures in this paper are available online at http://ieeexplore.ieee.org.

Digital Object Identifier 10.1109/TMAG.2015.2474123

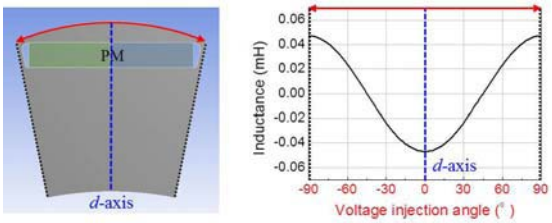

Fig. 1. Inductance waveform of d-axis with high-frequency voltage injection.

In this paper, the basic principle of the saliency-based sensorless control is discussed, and two methods are proposed to estimate the rotor position. The first method is the contour plotting of the inductances of the d-axis and q-axis varied with rotor position, and the second method is evaluating the total harmonic distortion (THD) of the phase inductances. By using the proposed methods, the influence of the design parameters in the stator on the sensorless control feasibility is analyzed. Thus, the goal of this paper is to propose a design method of the concentrated winding sensorless-oriented machines that can achieve excellent sensorless drive performances.

II. Saliency-Based Sensorless Drive Feasibility

A. Basic Principle of Saliency-Based Sensorless Control

In an IPMSM, PMs have an effect on not only BEMF but also spatial saliency distribution. Nonuniformly positioned PM in the rotor causes a discrepancy between the reluctance of d-axis and the reluctance of q-axis. This result brings about the spatial saliency. Thus, with a pulsating high-frequency voltage signal injection, the position of the rotor can be estimated based on the saliency [2]. As shown in Fig. 1, if the voltage injection angle is 0° when the voltage is injected into the d-axis, the self-inductance of d-axis has a minimum value and the mutual inductances of d-axis and q-axis must be zero-crossing. Thus, the rotor position can be estimated by measuring the variation of the inductance or the current response.

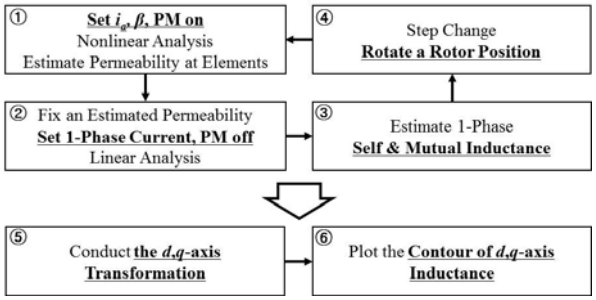

Fig. 2. Simulation process to estimate rotor position.

B. Method 1: Contour of Inductance and Estimation Error

However, the inductance and current responses are distorted with the rotor position by the saturation of the core or the cross-saturation effect. Thus, a certain simulation process has to be carried out, as shown in Fig. 2, to estimate the rotor position.

1) Nonlinear finite-element analysis (FEA) is conducted including PMs to take into consideration the saturation of the core under the load conditions.
2) The next step involves fixing the permeability at each mesh decided in the first step, converting the residual induction of the PM to 0, and performing linear FEA by applying the unit current to the coil of a single phase.
3) Three-phase self-inductance and mutual inductance can be obtained as linkage flux per unit current.
4) The procedure is iterated with the rotor position for one period in the electrical angle.
5) Self-inductance and mutual inductance of d- and q-axes can be calculated through axis transformation.
6) The contour plot of the mutual inductances of the d-axis and q-axis to estimate rotor position is obtained.

Consequently, the rotor position can be estimated by contour plotting zero-crossing of the mutual inductances of the d- and q-axes varied with rotor position [5]. In this process, the saturation effect by the injected signal can be neglected, since its magnitude is much smaller and frequency is much higher than those of the main input voltage and current [9], [10].

C. Method 2: Inductance Harmonics and Estimation Error

In a way simpler than method 1, the effect of the inductance harmonics on the estimation error can be examined mathematically, whereas various harmonic components are mixed with the fundamental component in actual inductance, and each harmonic term of the three-phase inductances, L_{abch}, is expressed as (1) to analytically determine the effect of the nth harmonics on the inductances of d- and q-axes [9]. n is the harmonic order of the phase inductances, and L_h is an unknown value, as the magnitude of the nth harmonic

$$L_{abch} = L_h \begin{bmatrix} \cos 2\theta_r n & \cos 2n\left(\theta_r - \frac{\pi}{3}\right) & \cos 2n\left(\theta_r + \frac{\pi}{3}\right) \\ \cos 2n\left(\theta_r - \frac{\pi}{3}\right) & \cos 2n\left(\theta_r + \frac{\pi}{3}\right) & \cos 2\theta_r n \\ \cos 2n\left(\theta_r + \frac{\pi}{3}\right) & \cos 2\theta_r n & \cos 2n\left(\theta_r - \frac{\pi}{3}\right) \end{bmatrix}. \quad (1)$$

TABLE I
RELATION BETWEEN HARMONIC ORDERS OF PHASE INDUCTANCES AND MUTUAL INDUCTANCES OF d- AND q-AXES

n	2	4	5	7	8	10	11	13	…
m	1	1	2	2	3	3	4	4	…
L^r_{dqh}	6	6	12	12	18	18	24	24	$6k$-th

The three-phase inductance matrix can be transformed into the inductance matrix of the d- and q-axes using [9]

$$L^r_{dqh} = \frac{3}{2} T_{\theta_r} T_{dq} L_{abch} \left(T_{\theta_r} T_{dq}\right)^T \quad (2)$$

where T_{dq} and $T_{\theta r}$ are the d- and q-axes and rotational transform coefficients relatively. L_d, L_q, L_{dq}, and L_{qd} are the self- and mutual inductances of the d- and q-axes.

The inductance of d- and q-axes, L^r_{dqh}, caused by the nth harmonic of the phase inductance can be obtained using (1) and (2)

$$\begin{aligned} L^r_{dqh} &= \frac{3}{2} L_h \begin{bmatrix} \cos 6\theta_r m & -\sin 6\theta_r m \\ -\sin 6\theta_r m & -\cos 6\theta_r m \end{bmatrix} && \text{at } n = 3m-1 \\ L^r_{dqh} &= \frac{3}{2} L_h \begin{bmatrix} \cos 6\theta_r m & \sin 6\theta_r m \\ \sin 6\theta_r m & -\cos 6\theta_r m \end{bmatrix} && \text{at } n = 3m+1 \\ L^r_{dqh} &= 0 && \text{at } n = 3m \end{aligned} \quad (3)$$

where m is the natural number. As described in (3), the harmonics of the phase inductances, except the $3k$th harmonic terms, cause the $6k$th periodic ripple of the inductances of d- and q-axes varied with the rotor position during one period in the electrical angle ($k = 1, 2, 3, \ldots$). The relation between the harmonics of the phase inductances and the inductances of d- and q-axes can be organized, as shown in Table I. Thus, the magnitude of the estimation error is represented by examining the THD of the phase inductances excluding the $3k$th harmonic terms (THD_L). THD_L should be calculated by using the phase inductances obtained from nonlinear FEA, considering both the armature reaction and the operating point of the PMs.

III. INITIAL MODEL AND ANALYSIS OF DESIGN PARAMETERS

In this paper, design parameters, such as chamfer, closed slot, and notch, were analyzed to design sensorless-controlled concentrated winding IPMSM. The configurations of considered models are shown in Fig. 3. The parameters were analyzed by using the proposed methods. Based on the analysis results of the models, as shown in Fig. 4, one of the proposed models was manufactured and tested.

A. Initial Model

The 115 Nm 14 kW initial model for EV traction is shown in Fig. 3(a). The diameter and the stack length of the motor are 274 and 70 mm. The thickness of the tooth tip is 1.5 mm. Maximum input voltage and current are 320 $V_{\rm dc}$ and 100 $A_{\rm rms}$. The magnitude and the THD of the phase BEMF at 1000 r/min are 41.38 $V_{\rm rms}$ and 5.86%. The saliency ratio is 1.75. THD_L and the peak-to-peak estimation error under the full load condition are 24.97% and 13.25°, respectively, as shown in Fig. 4(a).

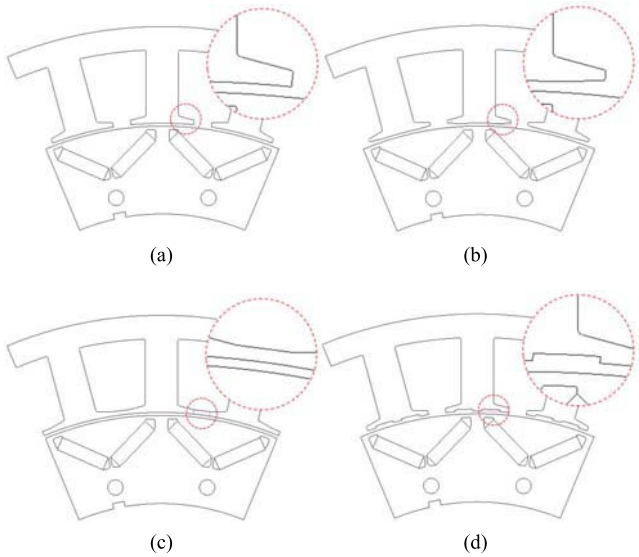

Fig. 3. Configuration of the 16-pole 24-slot analysis models. (a) Initial model. (b) Chamfer. (c) Closed slot. (d) Notch.

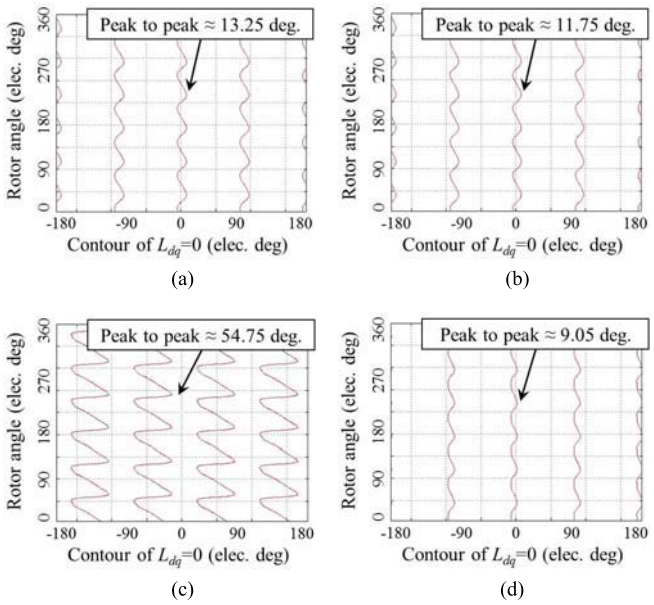

Fig. 4. Estimated rotor position of the proposed models. (a) Initial model (THD_L: 24.97%). (b) Chamfer (THD_L: 22.61%). (c) Closed slot (THD_L: 142.05%). (d) Notch (THD_L: 14.99%).

B. Chamfer

The second model applied with the chamfer is shown in Fig. 3(b). The thickness of the tooth tip is 1 mm. The magnitude and the THD of the phase BEMF at 1000 r/min are 41.20 $V_{\rm rms}$ and 3.78%. The saliency ratio is 1.72. THD_L and the peak-to-peak estimation error under the full load condition are 22.61% and 11.75°, as shown in Fig. 4(b). In the analysis results, both the sensorless drive feasibility and the THD of the BEMF are improved. This is because the tooth-tip leakage inductance is decreased. Also, the magnitude of the BEMF is decreased merely 0.18 $V_{\rm rms}$.

C. Closed Slot

The third model applied with the closed slot is shown in Fig. 3(c). The magnitude and the THD of the phase BEMF at 1000 r/min are 36.23 $V_{\rm rms}$ and 1.98%. The saliency ratio is 1.49. THD_L and the peak-to-peak estimation error under the full load condition are 142.05% and 54.75°, as shown in Fig. 4(c). As shown in the results, it has a significantly negative effect on the saliency-based sensorless drive. The magnetic flux produced by the armature current flows only in the stator through the closed tooth tip at certain rotor positions. In other words, the tooth-tip leakage inductance is very high. Fig. 5 shows the comparison of the equipotential lines in the initial model and the closed slot model at certain rotor positions. For this reason, the self-inductance is rapidly increased and decreased before and after the rotor positions. Therefore, the inductance is distorted severely, resulting in large estimated rotor position error.

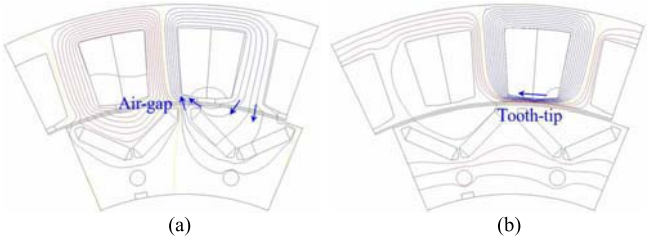

Fig. 5. Equipotential line at 3.5° rotor position in mechanical angle. (a) Initial model. (b) Closed slot.

D. Notch

The last model applied with the notch is shown in Fig. 3(d). The width of the notch is the same with the slot open, and the depth is 0.4 mm. The magnitude and the THD of the phase BEMF at 1000 r/min are 38.93 $V_{\rm rms}$ and 11%. The saliency ratio is 1.63. THD_L and the peak-to-peak estimation error under the full load condition are 14.99% and 9.05°, as shown in Fig. 4(d). In this case, the notch at the tooth tip decreases tooth-tip leakage flux and results in small estimation error. In contrast, the BEMF is largely decreased and deteriorated.

IV. Final Model and Experimental Verifications

The goal of the proposed design procedure is not only the reduction of the estimation error but also the achievement of the required torque. Based on the analysis results in Section III, the estimation error can be decreased by applying the chamfer or the notch to the stator. However, the magnitude of the phase BEMF is relatively much more decreased by the notch in the stator. Therefore, the stator chamfer was selected as the optimum design parameter, and the model in Fig. 4(b) was chosen as a final proposed IPMSM for sensorless drive.

The final model was tested to verify the validity of the proposed analysis methods and the design results. A load machine, a torque sensor, and the test motor were connected mechanically in series in the experiment setup. The test was conducted by the sensorless drive using analog filter circuit, and the switching frequency of the driver was 16.5 kHz [10]. Fig. 6 shows the current response obtained from the experiment under the full load condition. The six-periodic ripple was mainly caused by the second and fourth harmonics of L_a,

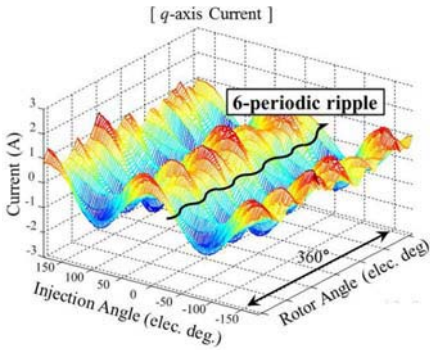

Fig. 6. Current ripple of q-axis caused by the second and fourth inductance harmonics.

TABLE II
AVERAGE POSITION ERROR OF LAST MODEL

Speed (rpm)	q-axis current				
	140 A_{peak}	98 A_{peak}	0 A_{peak}	-98 A_{peak}	-140 A_{peak}
0	-1.3 deg.	1.3 deg.	0.9 deg.	0.7 deg.	0.9 deg.
200	-1.3 deg.	0.4 deg.	1.9 deg.	1.0 deg.	-1.1 deg.

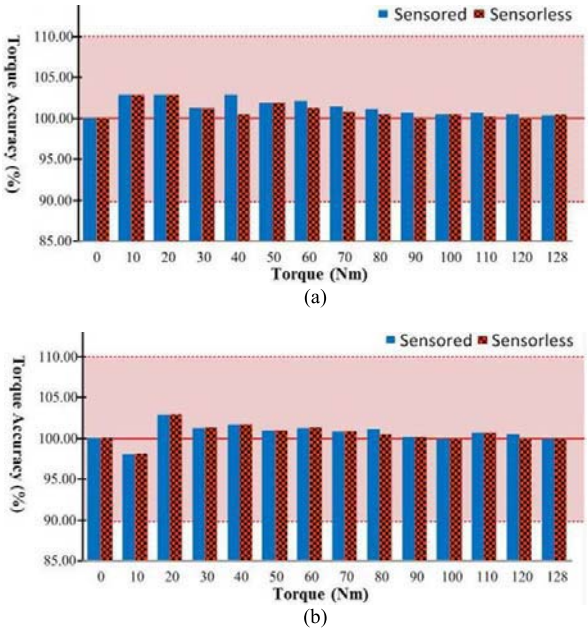

Fig. 7. Torque accuracy test results. (a) 100 r/min. (b) 200 r/min.

as shown in Table I and Fig. 4. Table II demonstrates that the average values of the estimated rotor position errors were experimentally determined 0.9° to 1.9° at 0 and 200 r/min. Lastly, Fig. 7 shows the torque test results of sensored and sensorless drive at 100 and 200 r/min, respectively. The reason that 2.5% error occurs at the 10 Nm is the torque ripple, and the coupling misalignment has large effects on the measurement during the load test, since it had low speed and low torque condition. However, the discrepancies between the torque accuracies are not over 2.5%, and the torque accuracy is almost 100% in all the desired torque operations. In conclusion, the IPMSM achieved both excellent sensorless drive performance and the required torque through the proposed design procedure.

V. CONCLUSION

In this paper, two analysis methods were proposed to investigate the effect of the stator design parameters on sensorless drive feasibility. By using these methods, it was confirmed that the estimated rotor position error can be decreased by applying the chamfer or the notch to the stator. To achieve excellent sensorless drive performance as well as the required specifications, the machine applied with the stator chamfer was proposed as the final model. Through the experiments of the proposed model, it was verified that the estimation error at very low speed is small enough to achieve almost 100% torque accuracy in all the desired torque operations. Thus, it can be concluded that the proposed methods to analyze the design parameters and the design results are useful for achieving great saliency-based sensorless drive performance of the concentrated winding IPMSM for EV traction.

ACKNOWLEDGMENT

This work was supported in part by the Korean Agency for Defense Development, in part by the Ministry of Science, ICT and Future Planning (MSIP), Korea, under Grant 1415123341, and in part by the MSIP within the Convergence Information Technology Research Center under Grant IITP-2015-H8601-15-1005 supervised by the Institute for Information and Communication Technology Promotion and a Research Program entitled The Specialized Research Center on the Future Ground System.

REFERENCES

[1] K. I. Laskaris and A. G. Kladas, "Internal permanent magnet motor design for electric vehicle drive," *IEEE Trans. Ind. Electron.*, vol. 57, no. 1, pp. 138–145, Jan. 2010.
[2] S. Kim, J.-I. Ha, and S.-K. Sul, "PWM switching frequency signal injection sensorless method in IPMSM," *IEEE Trans. Ind. Appl.*, vol. 48, no. 5, pp. 1576–1587, Sep./Oct. 2012.
[3] Y. Kano, T. Kosaka, N. Matsui, and M. Fujitsuna, "Sensorless-oriented design of concentrated-winding IPM motors for HEV drive application," in *Proc. 20th ICEM*, Marseille, France, Sep. 2012, pp. 2709–2715.
[4] Y. Li, Z. Q. Zhu, D. Howe, and C. M. Bingham, "Modeling of cross-coupling magnetic saturation in signal-injection-based sensorless control of permanent-magnet brushless AC motors," *IEEE Trans. Magn.*, vol. 43, no. 6, pp. 2552–2554, Jun. 2007.
[5] Z. Q. Zhu, Y. Li, D. Howe, and C. M. Bingham, "Compensation for rotor position estimation error due to cross-coupling magnetic saturation in signal injection based sensorless control of PM brushless AC motors," in *Proc. IEMDC*, Antalya, Turkey, May 2007, pp. 208–213.
[6] N. Bianchi and S. Bolognani, "Influence of rotor geometry of an IPM motor on sensorless control feasibility," *IEEE Trans. Ind. Appl.*, vol. 43, no. 1, pp. 87–96, Jan./Feb. 2007.
[7] P. Sergeant, F. De Belie, and J. Melkebeek, "Rotor geometry design of interior PMSMs with and without flux barriers for more accurate sensorless control," *IEEE Trans. Ind. Electron.*, vol. 59, no. 6, pp. 2457–2465, Jun. 2012.
[8] M.-S. Lim, S.-H. Chai, and J.-P. Hong, "Design and iron loss analysis of sensorless-controlled interior permanent magnet synchronous motors with concentrated winding," *IET Electr. Power Appl.*, vol. 8, no. 9, pp. 349–356, Nov. 2014.
[9] S.-H. Chai, B.-H. Lee, J.-P. Hong, S.-K. Sul, and S.-M. Kim, "Design of IPMSM having high power density for position sensorless operation with high-frequency signal injection and the method of calculating inductance profile," in *Proc. ICEMS*, Beijing, China, Aug. 2011, pp. 1–5.
[10] S. Jung and J.-I. Ha, "Sensorless control of AC machines at carrier frequency signal injection using analog filter circuit," in *Proc. PEDS*, Kitakyushu, Japan, Apr. 2013, pp. 439–444.